Journal of Materials Research and Technology 33 (2024) 8071–8078

Contents lists available at ScienceDirect

Journal of Materials Research and Technology

journal homepage: www.elsevier.com/locate/jmrt

Brittle fracture of notched components fabricated by stereolithography

Mohammad Reza Khosravani [a,*], Peter Frohn-Sörensen [b], Andreas Schwarzkopf [a], Bernd Engel [b], Tamara Reinicke [a]

[a] Chair of Product Development, University of Siegen, Paul-Bonatz-Str. 9-11, 57068 Siegen, Germany
[b] Forming Technology Siegen, University of Siegen, Breite Strasse 11, 57076 Siegen, Germany

ARTICLE INFO

Keywords:
3D printing
Fracture
V-notch
SLA
FEM
DIC

ABSTRACT

Since additive manufacturing (AM, i.e., 3D printing) has been widely used for production of end-used products, the mechanical strength of parts fabricated by this technology have gained considerable significance. The current study presents fracture load assessment of 3D-printed components fabricated by the stereolithography (SLA) technique using UV sensitive resin material. In this context, dumbbell-shaped specimens were printed and tested to determine basic mechanical properties. Moreover, V-notched semi-circular bending test coupons with various notch opening angles (i.e., 15°, 30°, 45°, 60°, 75°, and 90°) were printed and examined. Parallel to the experimental tests, we developed a finite element model to simulate the load carrying performance of 3D-printed parts. Moreover, we used the digital image correlation technique to determine displacement and strain field on the surface of the examined specimens. Since the mechanical strength and fracture behavior of 3D-printed parts are investigated in the current study, the presented outcomes can be utilized for innovative designs of parts fabricated by SLA with a higher mechanical strength, and improved load-carrying capacity.

1. Introduction

Development and applications of additive manufacturing (AM) has led to new innovative designs. AM, also known as three-dimensional (3D) printing proved its advantages compared to traditional manufacturing processes. 3D printing refers to fabrication of prototypes or final products from a 3D digital model [1]. Several advantages of 3D printing such as design flexibility, reduces machine set-up times, and minimal material waste, have led to various applications of this manufacturing process. For instance, 3D printing has been utilized for fabrication of instruments, structural elements, and tools in different fields [2–5]. According to ISO/ASTM 52900 [6], 3D printing has been classified into seven techniques and stereolithography (SLA) is employed in this study.

Vat photopolymerization is a type of 3D printing method that uses a light source for curing the photocurable resin in a vat. In this context, the most popular techniques are: (i) SLA printing and (ii) digital light processing (DLP). The SLA utilizes a high-powered laser for hardening of liquid resin, but DLP uses light emitting diode for polymerization of the layer [7]. Considering the benefits, SLA has acquired broad attention in different fields, such as biomedical engineering, jewelry, nanocomposites, and fabrication of metamaterial components [8–10]. Although previous research works confirmed that the orientation during 3D printing has influence on the mechanical behavior of 3D-printd parts [11–14], this printing parameter has a little impact on the mechanical characteristics of SLA 3D-printed components. In [15], optimizations were performed in biomedical resin for vat photopolymerization technique. In a study by Hague et al. [16], tensile, flexural, and impact properties of SLA parts printed with different orientations were determined. The documented results showed that effects of printing direction on the mechanical behavior of SLA part is less than 5%. Later, in the works of Quintan et al. [17] and Stoegerer et al. [18], effects of printing direction on the mechanical properties of SLA parts were investigated. The outcome of these studies confirmed that the mechanical properties and strength of SLA 3D-printed parts are not affected by printing orientation. Therefore, SLA method can be used for fabrication of isotropic parts.

Since currently 3D printing is widely utilized for fabrication of end-use products, the mechanical strength and the fracture behavior of 3D-printed parts are of significant importance. In this context, several studies have been performed to investigate fracture of 3D-printed parts [19–22]. In the work of Kiendl and Gao [23], the raster layup as a 3D printing parameter was used to control the strength and toughness of 3D-printed polymer parts. The experiments indicated that a higher toughness can be obtained when the specimen is loaded diagonally to the raster direction compared to parallel or perpendicular loading conditions. Later, we investigated the brittle fracture in the cracked square plate specimens fabricated by SLA technique [24]. Particularly,

* Corresponding author.
E-mail address: mohammadreza.khosravani@uni-siegen.de (M.R. Khosravani).

https://doi.org/10.1016/j.jmrt.2024.11.052
Received 19 July 2024; Accepted 6 November 2024
Available online 16 November 2024

the specimens with different crack orientation angles were 3D-printed and based on the experimental tests their fracture behavior and crack propagation were determined. The findings showed that only in pure mode I, the crack was propagated in the same direction as the initial crack. In investigation of the fracture in the structural elements, the semi-circular bending (SCB) specimens were initially proposed in [25]. Using the SCB specimens has some advantages. For example, the required material is relatively small and test by SCB samples does not require any special equipment or loading jig for the fracture test. Therefore, SCB specimens have been employed in different research works over the years [26–29]. Moreover, compact tension (CT) test is currently used as a common method for fracture studies of different materials [30–32]. CT test has some advantages compared to other techniques. For example, the specimen in CT test requires less material. In this investigation, we employed SCB specimens and CT test due to their aforementioned benefits.

The aim of the present study is to determine fracture behavior and mechanical strength of notched 3D-printed parts. As the main novelty of this research, it is revealed that notched parts and J-integral method can be used to determine fracture behavior of SLA 3D-printed parts. In this context, SLA technique is utilized and V-notched SCB specimens with different notch opening angles are 3D-printed. Particularly, the specimens with angle ranging from 15° to 90° with a 15° increment are fabricated and tested. The dumbbell-shaped samples and CT test coupons are fabricated and examined to determine basic mechanical properties. In the experimental tests, digital image correlation (DIC) technique is used, which is a non-contact optical measurement approach to measure strain from the local deformation on the surface of specimens and strain distributions at crack tips. Parallel to the experimental practises, stress distributions are investigated on the finite element (FE) models of the notched samples. The results can be utilized for further designs of 3D-printed components with optimized strength and improved mechanical performance. The structure of this paper is as follows: next section presents methodology and a brief overview of the theoretical background. Details of design and fabrication of test coupons are described in Section 3. In Section 4, experimental tests including tensile, CT, and three-point bending tests are explained. Section 5 presents verification of tests by FE model and DIC technique. The obtained results are presented and discussed in Section 6. Finally, a short summary of the current study is outlined in Section 7.

2. Methodology and theoretical background

A notch causes a stress concentration that can leads to the initiation of cracks. Therefore, notches are commonly used to determine fracture mechanics related properties. In fact, cracks initiated from sharp notches, therefore notches play important role in mechanical strength of the parts. In this study, we used 3D-printed specimens with notches, which are suitable to investigate the fracture behavior. A review of literature reveals that V-notches have gained popularity in investigation of fracture behavior compared to other types of notches. This can be related to their applications in different mechanical components, like bolts and screws, as well as their higher stress concentration compared to other notches (e.g., rectangular, U- and O-notches).

In the field of fracture mechanics, the J-integral method is a well-known method that has been recommended for evaluation of the fracture toughness in notched [33] or cracked [34] test coupons with elastic–plastic or elastic behavior. According to the J-integral method, fracture initiation happens when the parameter reaches its critical value (J_c). The following equation can be used to calculate the absolute values of the J-integral [35]:

$$J_k = \oint_{\Gamma} \left(W n_k - T_i \frac{\partial u_i}{\partial x_k} ds \right) \quad (K = 1, 2) \tag{1}$$

where J_k is the value of J-integral. In addition, W and n_k indicate strain energy density and the unit vector normal to the certain contour path (Γ), respectively. Moreover, T_i and u_i denote the indicatives of the traction and displacement vector, respectively. A Cartesian coordination system (two axes: parallel and perpendicular to the crack direction) can be taken into account. Based on Eqs. (2) and (3), the values of J-integral can be evaluated along the Cartesian coordination system. In addition, Eq. (4) can be used to determine equivalent J-integral:

$$J_1 = \int_{\Gamma} \left(W d_y - T_i \frac{\partial u_i}{\partial_x} ds \right) \tag{2}$$

$$J_1 = \int_{\Gamma} \left(W d_x - T_i \frac{\partial u_i}{\partial_y} ds \right) \tag{3}$$

$$J_{eq} = \sqrt{J_1^2 + J_2^2} \tag{4}$$

In [36], cohesive zone model was used to study the fracture behavior of sharp V-notched specimens based on four-point bending tests. Later, Carpinteri et al. [37], employed finite fracture mechanics criterion to predict failure of structures with sharp V-notches. In the aforementioned studies, the researchers used numerical simulation to predict the fracture, but in the present study we used not only numerical approaches, but also DIC technique is used to assess the failure of sharp V-notched 3D-printed components.

3. Design and printing of specimens

In the present study, three groups of the specimens were designed and fabricated: (i) dumbbell-shaped (ii) CT, and (iii) V-notched SCB specimens. The dumbbell-shaped and CT test coupons were designed according to ASTM D638-14 [38] and ASTM D5045-14 [39], respectively. Fig. 1 shows the schematics of the fabricated specimens. The SCB specimens were designed with different angles 2α of 15°, 30°, 45°, 60°, 75° and 90°. All specimens were designed in Siemens NX [40] and exported as STL files to use for fabrication based on the SLA technique.

These STL files were sliced using the Chitubox Slicer [41]. All 3D-printed specimens were executed with the same process parameters and ambient conditions. The layer height was set to 0.05 mm and the exposure time for every regular layer was 8 s. An Elegoo Saturn 8k SLA 3D printer with a display resolution of 28 μm was used. In this study, we used "3D Printing UV sensitive Resin – Basic (gray)" material, produced by Shenzen Anycubic Technology Co., Ltd [42]. The resin was shaken well before 3D printing, as recommended by the manufacturer. For the printing process, the 3D printer was placed in an enclosure. The enclosure was heated to meet the recommended temperature of the resin manufacturer. Therefore, the enclosure was preheated to 28 °C and the temperature was held over the whole printing process. After printing process, the supports were removed and the same cleaning routine was executed for all specimens. In the first step, the specimens were pre-cleaned in an isopropanol bath. In the second step, the specimens were cleaned in an Elegoo Mercury X wash machine with isopropanol. The used isopropanol for both cleaning steps was technical isopropanol with a minimum purity of 98%. Finally, all specimens were post-cured from two opposite sides to ensure uniform post-curing, whereby each side was cured for 20 min in an Elegoo Mercury X Cure machine. Prior to the tests, we used a razor blade to provide a sharp notch tip in all V-notched SCB specimens.

4. Experimental tests

4.1. Tensile tests of 3D-printed dumbbell-shaped and CT specimens

In the first part of the experiments, the dumbbell-shaped specimens experienced the tensile loads according to ASTM D638-14 [38]. Particularly, we utilized Zwick/Roell Z250 uniaxial testing machine that has a wide measurement range and can precisely determine small forces. All tensile experiments were performed at a ramp displacement of 0.5 mm/min. Fig. 2 shows a dumbbell-shaped specimen under

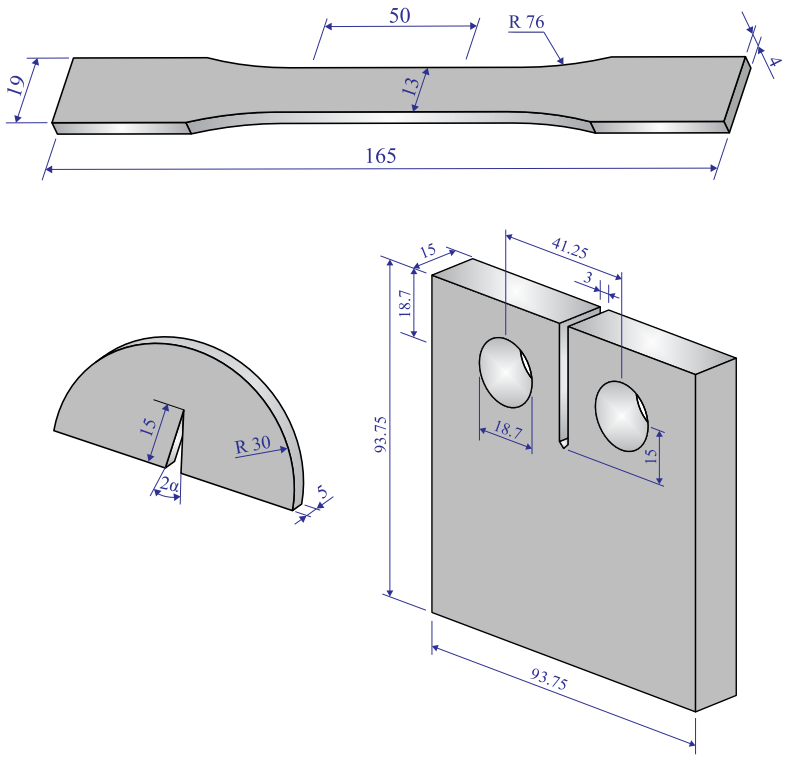

Fig. 1. Schematics of designed and fabricated specimens: Dumbbell-shaped, CT, and V-notched semi-circular bending specimens (all dimensions in mm).

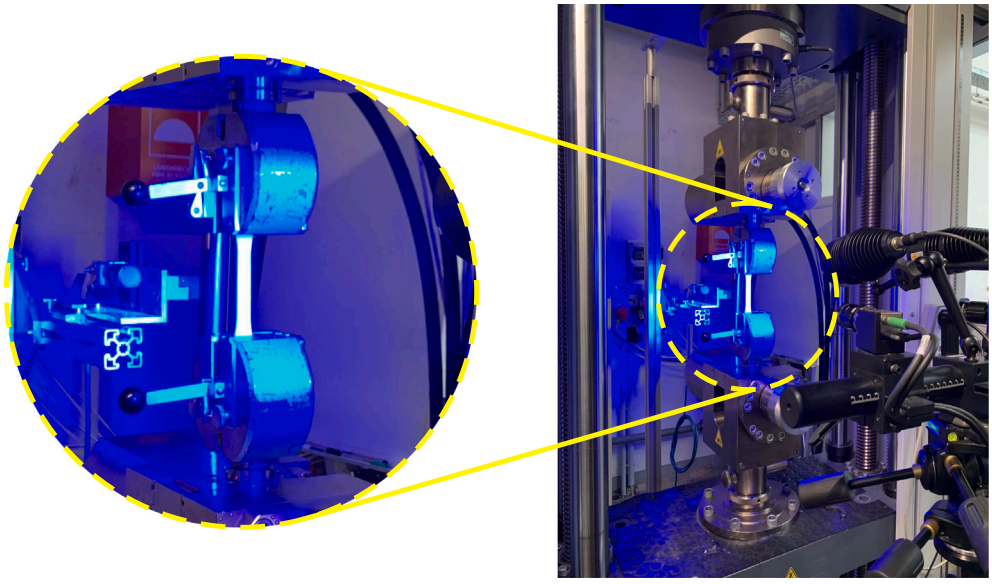

Fig. 2. A 3D-printed dumbbell-shaped samples under tensile test conditions.

tensile test conditions. Based on the tensile tests, the basic mechanical properties (e.g., tensile strength) were determined and utilized in FE simulations. It is noteworthy that DIC technique has been used to observe strain and displacement of the dumbbell-shaped specimens. In fact, we used DIC to record changes in the strain of the front surface of the specimens under tensile load. The strain field and displacement are determined by dividing the images into a block of pixel (subset) and tracking the movement to the neighbor subsets. For this reason, an unique pattern is required, which has been called a speckle pattern. Here, the dumbbell-shaped samples were spray-painted before DIC. To this aim, a white base coat layer was provided and then a graphite based paint system was used to create a black stochastic speckle pattern. Here, we used a GOM ARAMIS 12M Adjustable camera system and virtual extensometer with gauge length of 50 mm for tensile testing.

It should be noted that all tensile tests were performed at room temperature (RT) conditions: 23 ± 3 °C and 50 ± 5% temperature and relative humidity, respectively. We conducted tensile tests on five dumbbell-shaped test coupons and reproducibility of the results is confirmed.

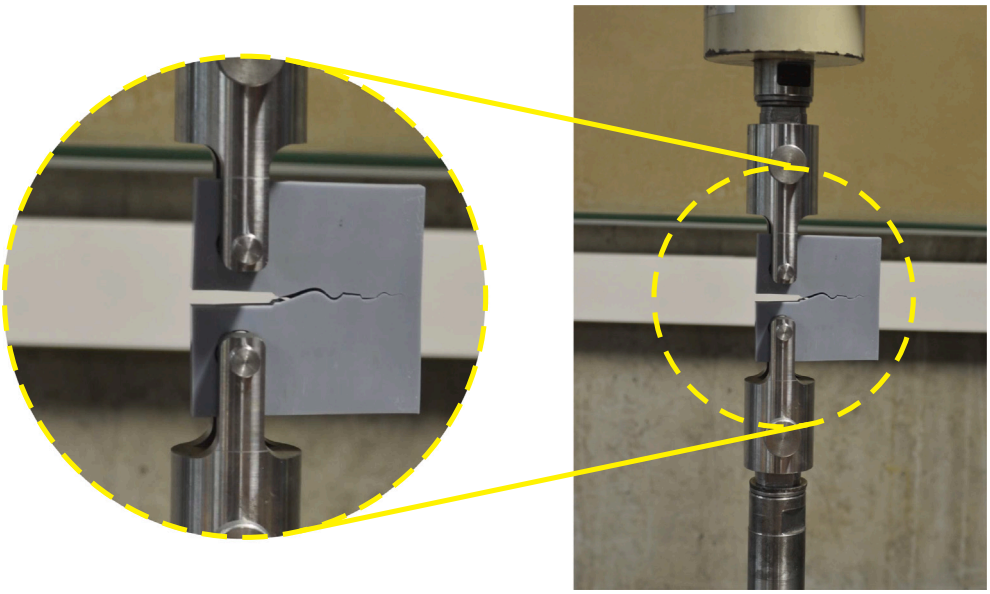

Fig. 3. A fractured 3D-printed CT specimen on the testing machine.

Moreover, the fracture tests are performed on CT specimens to determine fracture toughness using the J-integral method. In this context, CT specimens were subjected to the tensile load utilizing testing fixture in a hydraulic machine, which is fitted with a 15 kN load cell. In this study, we have designed and prepared a fixture that has identical upper and lower grips. The grips were attached to the CT specimen by a clevis pin arrangement. It should be noted that during the set-up, two grips were positioned in alignment and fastened there with a pre-load.

The utilized machine has as cross-head speed range of 0.01 to 30 mm/s and all tests were performed under displacement control conditions with a constant displacement rate of 10 mm/min according to ASTM D5045-14 [39]. We tested four CT specimens and a fractured CT specimen after test is illustrated in Fig. 3.

Since ambient temperature has effect on the physical properties of materials, all CT tests were performed at RT conditions similar to the tensile tests of dumbbell-shaped samples.

4.2. Three-point bending tests of 3D-printed V-notched SCB samples

A series of three-point bending tests was carried out on the V-notched SCB specimens utilizing a Zwick/Roell Z250 uniaxial testing machine. The bending experiments were performed to study stress field in the vicinity of the notch in 3D-printed SLA specimens. The SCB test coupons were loaded by a vertical load via constant cross-head movement of 1 mm/min. Similar to the tensile tests on the dumbbell-shaped specimens, we used the DIC technique in three-point bending tests. To this end, all V-notched SCB samples were spray-painted to create a pattern of randomly spaced black dots that is needed to capture the strain maps. Fig. 4 shows a V-notched SCB specimen under three-point bending test conditions. Similar to aforementioned tensile and CT tests, all three-point bending tests were conducted at RT conditions. It should be noted that the span length was selected in such a way to satisfy $0.5 \leq s/D \leq 0.8$, where s and D are the distance between two supports and the specimen diameter, respectively. Here, horizontal distance between the lower supports is 32 mm.

It is worth mentioning that performing tests on four V-notched SCB specimens in each notch opening angle confirmed reproducibility and repeatability of the results.

5. Verification of experimental tests

This section presents applications of DIC and computational approach for verification of performed tests in the following subsections:

5.1. Verification of experimental tests by DIC

The experiments on tensile tests and SCB specimens were examined by the DIC technique. To this end, the gom ARAMIS Adjustable Base 12M equipment was used to capture strain maps during the experimental procedures. The system comprises two cameras with a resolution of 12 megapixels, LED illumination and a digital/analogue amplifier which is connected to a measurement computer as well as to the experimental machine channels, in this case the force and travel signals of the universal testing machine. This setup guarantees synchronized measurement of the experiment as well as strain capture from the specimen's surface. For the experiments of the present study, a calibration volume of $135 \times 100 \times 80$ mm^3 (length, width and depth) was utilized, which results in a local point distance of 16 pixels by using a facet size of 19 pixels. A calibration accuracy of 0.027 pixels was achieved for the camera system. The specimens were spray coated prior to the experiments using a matte white base coat followed by a stochastic spray pattern of a black graphite based spray paint. From this procedure, an average point count of in average circa 5100 points resulted for the SCB specimens. The experiments were conduced at RT.

For tensile testing of the dumbbell shaped specimens, uniaxial tensile strain was evaluated by a virtual extensometer (50 mm gauge length) to evaluate strain until fracture. For the SCB specimens, the strain maps at the frame before failure were evaluated, cf. Fig. 5. Even more, a circular evaluation area with a diameter of 2 mm was inserted at the tip of the V-notches to investigate the evolution of the local strain maximum from the experiment. For the SCB specimens, the displacement introduced to the experiments was tracked by the DIC equipment by means of reference points attached directly to the contact points of the three-point bending fixture. Doing so, any influence of the machine or assembly stiffness as well as clearances are excluded from the force–displacement curves.

5.2. Numerical analysis of SCB specimens under three-point bending tests

The three-point bending procedure of the SCB specimens is implemented into a numerical model for verification of the experimental procedure. To this aim, the computer-aided designed (CAD) data of the SCB specimens used for AM alongside with the three-point bending rig are imported into the CAE software Abaqus by Dassault Systemes, which is capable to perform numerical calculations based on the finite element method (FEM). Since the practical experiments on SCB

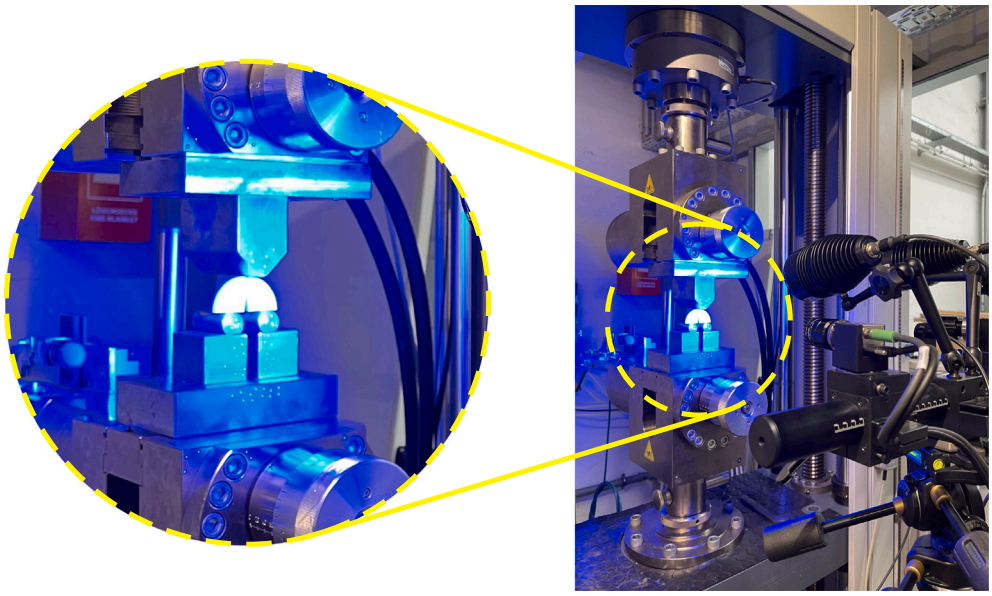

Fig. 4. A V-notched SCB specimen under test conditions with DIC setup.

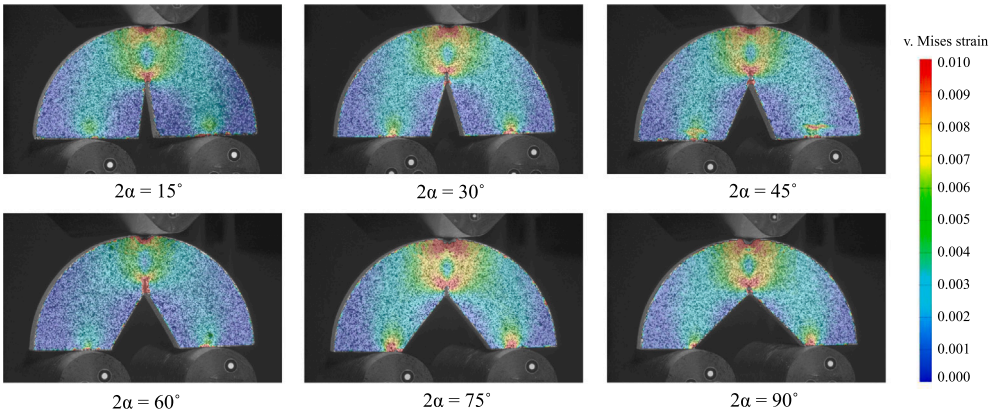

Fig. 5. Main DIC results from three-point-bending tests on SCB specimens under variation of notch angle. Depiction of equivalent strain maps with uniform scale of equivalent strain between 0 and 0.01 throughout images.

specimen indicated brittle fracture without signs of plasticity, the resin material of the SCB specimens is implemented by means of a density according to datasheet and its elastic behavior according to Table 1. It should be noted that despite the discontinuous progress in SLA process, herein modeled resin material is assumed isotropic, which is well-known to be valid as discussed in previous research works [16–18]. The three-point bending rig is represented by rigid tools since it is manufactured from steel and thus more than a hundredfold stiffer than the AM'ed resin material under consideration. The SCB specimens with varying notch angles are represented by a 0.5 mm mesh of hexagonal brick elements of linear geometric order, type C3D8R. The numerical representation of the three-point bending experiment is loaded according to the practical experiments with a position controlled, continuous displacement to initiate the bending load. At the interfaces between the supports of the test rig and the respective surfaces of the SCB specimens, contacts are modeled by a hard contact algorithm without penalty in orthogonal direction to surfaces and by a Coulomb's friction law in tangential direction. In this context, it shall be mentioned, that the lower supports are allowed to displace laterally to not obstruct opening of the angled notch of the SCB specimen. All other degrees of freedom (DOF) of the supports are fixed. The upper support's DOFs are fixed except for the vertical translation DOF, where a constant velocity of −0.2 mm/s is imposed. The numerical calculations are solved in an explicit approach until a fixed displacement of - 0.6 mm of the upper support of the fixture is achieved, which is well above the values observed during the experiments.

From these simulations, the stress maps at the specific displacement just before specimen failure are evaluated as numerical results, see Fig. 6. FEM provides the opportunity to visualize stress since there are few common experimental procedures, that allow direct evaluation of stress.

Furthermore, from this instance of time in simulation, the load being carried by each individual SCB specimen is evaluated and presented and compared in the results section of this paper. Besides of the quantitative comparison of the force maxima between FEM and practical experiments, the strain distribution obtained from DIC allows to verify the simulations in a qualitative way. To this aim, Fig. 7 shows the equivalent strain plots with respect to notch angle obtained from the conducted simulations. Evidently, these figures well agree to the strain plots obtained from the experiments, cf. Fig. 5.

The simulation model helps to evaluate the overall stiffness behavior of a notched component made from SLA resin. The stress distribution can be examined and optimized in any product application. If extended by a suitable failure model, an upgraded version of the simulation model may be considered to predict fracture of such a notched component.

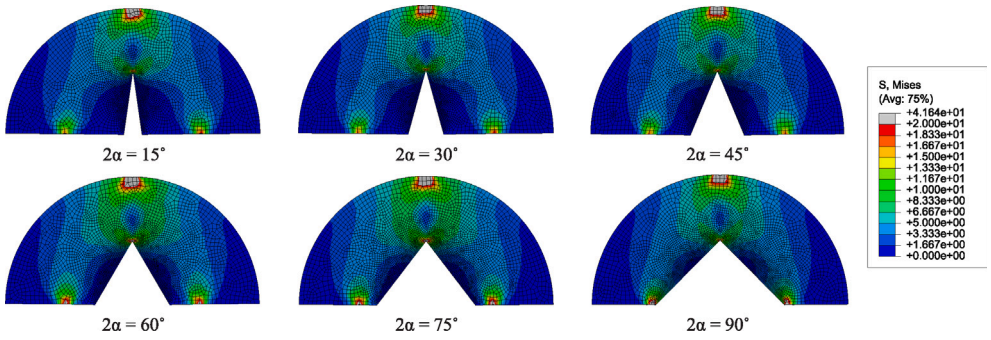

Fig. 6. Main FEM results from three-point-bending tests on SCB specimens with different notch angles. Depiction of v. Mises stress maps with uniform scale of stress between 0 and 20 MPa throughout images.

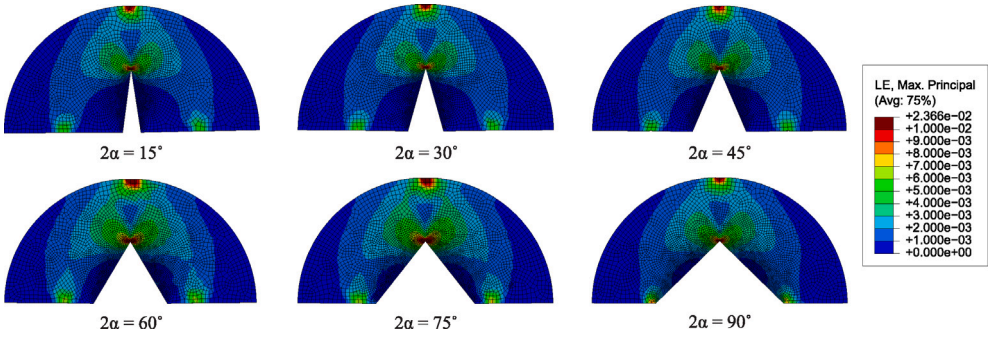

Fig. 7. Main FEM results from three-point-bending tests on SCB specimens with various notch angles. Depiction of major strain maps with uniform scale of strain between 0 and 0.01 throughout images.

Table 1
Tensile properties of tested dumbbell-shaped samples.

Tensile modulus E (MPa)	Ult. tensile strength S (MPa)	Fracture strain ϵ_f (%)
1458	20	13

6. Results and discussion

• Tensile and CT tests

During the tensile tests, an electronic control unit provides monitoring of the applied load and movement of the top cross head. The load–displacement curves were recorded for each test coupons. The critical load has been defined as the maximal load that corresponds to the onset of fracture. The fractures are within the gauge length (reduced section) in all dumbbell-shaped specimens, which confirm validity of the occurred failures. In Table 1 the obtained mechanical properties of examined dumbbell-shaped samples are summarized.

The CT specimens were tested in pure mode I loading, therefore the value of J_2 can be neglected, which means $J_{eq} = J_1$. Here, the fracture toughness (K_{IC}) is determined to be equal to 92.5 MPa (mm)$^{0.5}$ for the examined 3D-printed specimens.

• Three-point bending tests

During three-point bending tests, applied load and cross-head displacement were recorded. When a V-notched SCB specimen fails, fracture starts from the crack tip and the force drops from the peak. The average values of experimentally documented failure loads in the V-notched SCB specimens with different notch opening angles are presented in Fig. 8 and Table 2.

Here, the maximum tangential stress criterion is utilized to evaluate fracture of V-notched SCB 3D-printed specimens. According to this criterion, failure happens when the tangential stress reaches to its critical value at a certain distance near to the notch tip. In [43], the ultimate tensile strength is used as the critical value for the tangential stress. Based on the following equation, the value of the critical distance can be determined [37]:

$$r_c = \frac{1}{2\pi}\left(\frac{K_{IC}}{\sigma_u}\right)^2 \tag{5}$$

where K_{IC} and σ_u are fracture toughness and ultimate tensile strength, respectively. Considering the obtained fracture toughness and based on Eq. (5), the critical distance of examined V-notched SCB 3D-printed specimens is 0.072 mm.

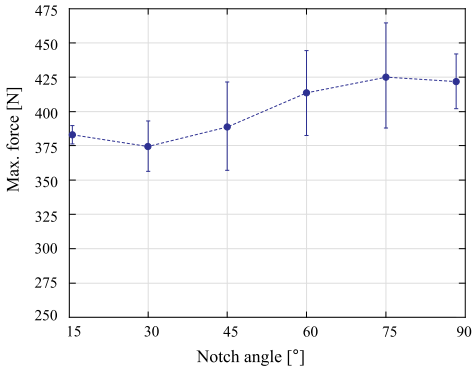

Fig. 8. Failure loads of the SCB specimens plotted as a function of notch angle.

Table 2
The average of failure loads in different V-notched SCB specimens.

	2α					
	15°	30°	45°	60°	75°	90°
F_{avg} (N)	383.4	373.3	390.8	413.4	424.7	422.5

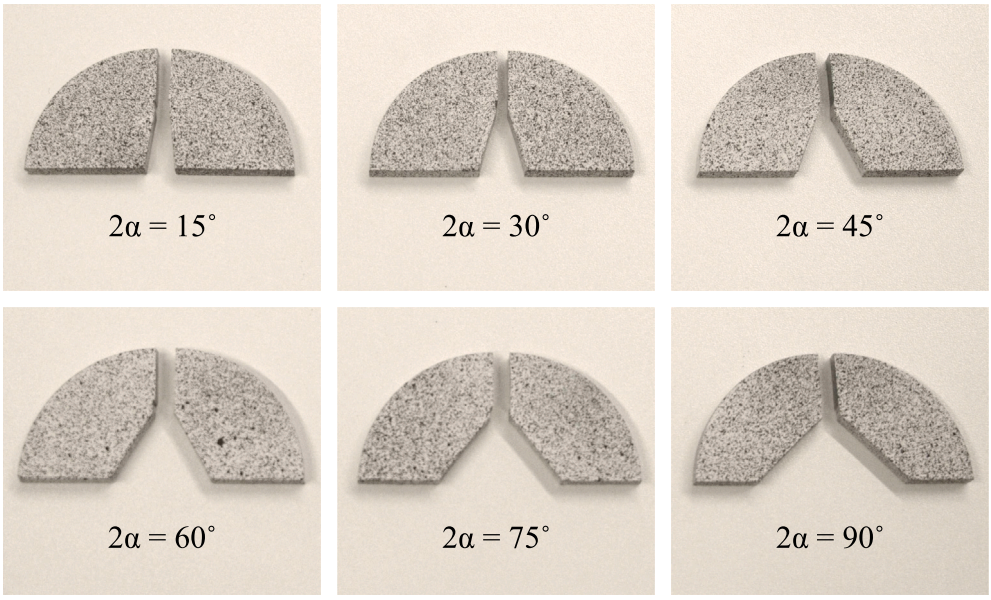

Fig. 9. Fractured V-notched SCB specimens with different notch opening angles.

Table 3
The average of failure loads obtained by experiments and DIC compared to the predicted values by the FE simulations.

2α	F_{avg} (N)		
	Experiments + DIC	FE simulations	Discrepancy (%)
15°	383.4	373.7	−2.53
30°	373.3	371.2	−0.56
45°	390.8	375.4	−3.94
60°	413.4	436.5	+ 5.59
75°	424.7	431.7	+ 1.65
90°	422.5	384.0	−9.11
			Absolute Avg = 4.40%

The fracture tests of V-notched SCB specimens indicated that the fracture started at the initial notch tip in all samples with different notch opening angles. Moreover, in all specimens, the crack propagates in the same direction of the original notch. The fractured test coupons with different notch opening angles are shown in Fig. 9. It should be mentioned that all specimens showed brittle fracture and none of the examined specimens had any signs of plasticity.

In Table 3, the average values of failure loads obtained experimentally in combination with the DIC technique and the predicted failure loads by FE simulations are summarized. As mentioned in the table, there is a discrepancy between experimentally obtained failure loads and failure loads predicted by FE simulations. This can be due to some differences in loading and boundary conditions in experiment and simulation, because not all actual conductions are assumed in FE simulations. For instance, in experimental practices there is a friction force between bottom supports and V-notched SCB specimens, but it is not considered in FE simulations. It is noteworthy that since test conditions are identical for the fracture test and DIC measurement, their discrepancy is low and they are in a good agreement.

Considering computational cost, convergence problems, and some disabilities of FE software in simulation of complex conditions, the DIC method can be used as a high-precision measurement for evaluation of load-bearing capacity of 3D-printed parts. In fact, DIC can be utilized to ensure that loading and boundary conditions are appropriately handled in the data collection and, consequently, in prediction of the fracture.

7. Summary and conclusions

In the present study, the mechanical strength and the fracture behavior of stereolithography (SLA) 3D-printed parts have been investigated. To this end, V-notched SCB specimens with different notch opening angles have been designed and printed. Moreover, dumbbell-shaped and compact tension (CT) test coupons have been fabricated and examined to determine the basic mechanical properties. Based on a series of three-point bending tests on the V-notched SCB specimens, effects of the notch opening angle on the failure load of specimens are determined. The V-notched semi-circular bending (SCB) specimens with a 75° notch opening angle had, in average, the highest failure load of 425 N. This value is reduced to 373 N for the specimens with 30° notch opening angle. Parallel to the experimental practices, finite element (FE) simulations are conducted to predict the failure loads in different specimens. The failure load of V-notched SCB specimens have been determined experimentally and predicted by FE simulations. The digital image correlation (DIC) technique was applied to evaluate strain maps from the specimen surfaces at failure and compared to the simulation results by qualitative means.

Comparison of the results indicate that there is a discrepancy between experimental results and FE simulation findings. Since some boundary conditions (e.g., effects of friction forces between supports and V-notched SCB specimens) are exist in experimental tests, but not assumed in FE simulations, there is a discrepancy between experiments and simulation results. On the other hand, comparison of experimentally obtained failure loads and measured failure load by DIC technique indicate a low discrepancy. In fact, since there are same test conditions for fracture test and DIC, the actual boundary conditions in the fracture tests are exist in the DIC. Therefore, there is a good agreement between experimental results and DIC measurement. Since different actual conditions (e.g., complex loading conditions, contacts) in real applications cannot be accurately simulated in FE software, the documented results confirm advantage of DIC technique compared to FE simulations in some applications. The outcome of the present study can be utilized for further numerical analysis, and improvement of strength in SLA 3D-printed components.

Declaration of competing interest

The authors declare that they have no known competing financial interests or personal relationships that could have appeared to influence the work reported in this paper.

References

[1] Gibson I, Rosen D, Stucker B, Khorasani M. Additive manufacturing technologies. Springer; 2021.
[2] Mantihal S, Kobun R, Lee BB. 3D food printingof as the new way of preparing food: A review. Int J Gastron Food Sci 2020;22:100260.
[3] Assi P, Achiche S, Laberge Lebel L. 3D printing process for textile composites. CIRP J Manuf Sci Technol 2021;32:507–16.
[4] Khosravani MR, Haghighi A. Large-scale automated additive construction: Overview, robotic solutions, sustainability, and future prospect. Sustainability 2022;14:9782.
[5] Daskalakis E, Hassan MH, Omar A, Cooper G, Weighman A, Bartolo P. Rheological behaviour of different composite materials for additive manufacturing of 3D bone scaffolds. CIRP J Manuf Sci Technol 2023;24:3670–82.
[6] ISO/ASTM-52900. Additive manufacturing - general principles - fundamentals and vocabulary. ASTM Int 2021.
[7] Zhang F, Zhu L, Li Z, Wang S, Shi J, Tang W, Li N, Yang J. The recent development of vat photopolymerization: A review. Addit Manuf 2021;22:102423.
[8] Vidakis N, Petousis M, Michailidis N, Papadakis V, Korlos A, Mountakis N, Argyros A. Multi-functional 3D-printed vat photopolymerization biomedical-grade resin reinforced with binary nano inclusions: The effect of cellulose nanofibers and antimicrobial nanoparticle agents. Polymers 2022;14:1903.
[9] Ferreira T, Almeida HA, Bartolo PJ, Campbell I. Additive manufacturing in jewellery design. In: ASME 11th biennial conference on engineering systems design and analysis. 2012, p. 187–94.
[10] Wang Y, Xu X, Liu S, Wang C, He Y, Sun C. Vat photopolymerization additive manufacturing. Elsevier; 2024, p. 407–37, [Chapter Vat photopolymerization 3D printing applications in metamaterials].
[11] Geng P, Zhao J, Gao Z, Wu W, Ye W, Li G, Qu H. Effects of printing parameters on the mechanical properties of high-performance polyphenylene sulfide three-dimensional printing. 3D Print Addit Manuf 2021;8:33–41.
[12] Khosravani MR, Soltani P, Reinicke T. Fracture and structural performance of adhesively bonded 3D-printed PETG single lap joints under different printing parameters. Theor Appl Fract Mech 2022;116:103087.
[13] Benamira M, Benhassine N, Ayad A, Dekhane A. Investigation of printing parameters effects on mechanical and failure properties of 3D printed PLA. Eng Fail Anal 2023;148:107218.
[14] Shan W, Liu P, Liang L, Liu Z, Bui TQ. A study on the effects of printing direction, grayscale and structure on performance of shape memory polymers (SMPs). Mater Today Commun 2024;38:108145.
[15] Vidakis N, Petousis M, Michailidis N, David C, Saltas V, Sagris D, Spiridaki M, Argyros A, Mountakis N, Papadakis V. Interpretation of the optimization course of silicon nitride nano-powder content in biomedical resins for vat photopolymerization additive manufacturing. Ceram Int 2024;50:14919–35.
[16] Hague R, Mansour S, Saleh N, Harris R. Materials analysis of stereolithography resins for use in rapid manufacturing. J Mater Sci 2004;39:2457–64.
[17] Quintana R, Choi JW, Puebla K, Wicker R. Effects of build orientation on tensile strength for stereolithography-manufactured ASTM D-638 type I specimens. Int J Adv Manuf Technol 2010;46:201–15.
[18] Stógerer J, Baumgartner S, Rath T, Stampfl J. Analysis of the mechanical anisotropy of stereolithographic 3D printed polymer composites. Eur J Mater 2022;2:12–32.
[19] Brugo TM, Campione I, Minak G. Investigation by digital image correlation of mixed-mode I and II fracture behavior of polymeric IASCB dpecimens with additive manufactured crack-like notch. Materials 2021;14:1084.
[20] Wang K, Cai R, Zhang Z, Liu J, Ahzi S, Peng Y, Rao Y. Compressive behaviors of 3D printed polypropylene-based composites at low and high strain rates. Polym Test 2021;103:107321.
[21] Khosravani MR, Bozic Z, Zolfagharian A, Reinicke T. Failure analysis of 3D-printed PLA components: Impact of manufacturing defects and thermal ageing. Eng Fail Anal 2022;136:106214.
[22] Tavara L, Madrigal C, Aranda MT, Justo J. Anisotropy and ageing effect on the mechanical behaviour of 3D-printed short carbon-fibre composite parts. Compos Struct 2023;321:117196.
[23] Kiendl J, Gao C. Controlling toughness and strength of FDM 3D-printed PLA components through the raster layup. Compos Struct 2020;180:107562.
[24] Khosravani MR, Frohn Sörensen P, Engel B, Reinicke T. Mixed mode brittle fracture of stereolithographic 3D-printed parts. J Mater Res Technol 2023;25:3177–88.
[25] Chong KP, Kuruppu MD. New specimen for fracture toughness determination for rock and other materials. Int J Fract 1984;26:59–62.
[26] Guo Q, Chen Z, Liu P, Li Y, Hu J, Gao Y, Li X. Influence of basalt fiber on mode I and II fracture properties of asphalt mixture at medium and low temperatures. Theor Appl Fract Mech 2021;112:102884.
[27] Zhang J, Zhang J, Cao D. Genetic algorithm optimization for cohesive zone modeling of viscoelastic asphalt mixture fracture based on SCB test. Eng Fract Mech 2022;271:108663.
[28] Khosravani MR, Anders D, Reinicke T. Effects of post-processing on the fracture behavior of surface-treated 3D-printed parts. CIRP J Manuf Sci Technol 2023;46:148–56.
[29] Xu Y, Zhao G, Li X, Wu B, Xia K. Influences of notch width and notch-tip angle on the fracture toughness measurement using the semi-circular bend (SCB) specimen. Eng Fract Mech 2023;281:109098.
[30] Brugo T, Palazzetti R, Ciric-Kostic S, Yan XT, Minak G, Zucchelli A. Fracture mechanics of laser sintered cracked polyamide for a new method to induce cracks by additive manufacturing. Polym Test 2016;50:301–8.
[31] Triclot J, Corre T, Gravouil A, Lazarus V. Key role of boundary conditions for the 2D modeling of crack propagation in linear elastic compact tension tests. Eng Fract Mech 2023;227:109012.
[32] Khosravani MR, Sadeghian H, Ayatollahi MR, Reinicke T. Optimization of fracture toughness in 3D-printed parts: Experiments and numerical simulations. Compos Struct 2024;329:117766.
[33] Chen YH, Lu TJ. On the path dependence of the J-integral in notch problems. Int J Solids Struct 2004;41:607–18.
[34] Khosravani MR, Reinicke T. Effects of printing parameters on the fracture toughness of 3D-printed polymer parts. Procedia Struct Integr 2023;47:454–9.
[35] Rice JR. A path independent integral and the approximate analysis of strain concentration by notches and cracks. J Appl Mech 1968;35:454–9.
[36] Gomez FJ, Elices M. A fracture criterion for sharp V-notched samples. Int J Fract 2003;123:163–75.
[37] Carpinteri A, Cometti P, Pugno N, Spora A, Taylor D. A finite fracture mechanics approach to structures with sharp V-notches. Eng Fract Mech 2008;75:1736–52.
[38] ASTM D638-14 standard test method for tensile properties of plastics. Standard, West Conshohocken, USA: American Society for Testing Materials; 2014.
[39] ASTM D5045-14 standard test method for plane-strain fracture toughness and strain energy release rate of plastic materials. Standard, West Conshohocken, USA: American Society for Testing Materials; 2014.
[40] Siemens. 2024, https://plm.sw.siemens.com. [Accessed 15 March 2024].
[41] CHITUBOX basic V2. 2024, https://www.chitubox.com/en/download/chitubox-free. [Accessed 15 March 2024].
[42] Farbiges UV resin. 2024, https://de.anycubic.com/products/farbiges-uv-resin. [Accessed 18 March 2024].
[43] Ayatollahi MR, Torabi AR, Bahrami B. On the necessity of using critical distance model in mixed mode brittle fracture prediction of V-notched Brazilian disk specimens under negative mode I conditions. Theor Appl Fract Mech 2016;84:38–48.